

Adaptive Reinforcement and Model Predictive Control Switching for Safe Human-Robot Cooperative Navigation

Ning Liu^a, Sen Shen^b, Zheng Li^a, Matthew D’Souza^c, Jen Jen Chung^{c,*},
Thomas Bräunl^a

^a*School of Engineering, The University of Western Australia, 35 Stirling Highway, Perth, 6009, WA, Australia*

^b*Department of Mechanical and Automation Engineering, The Chinese University of Hong Kong, Shatin, New Territories, Hong Kong SAR*

^c*School of Electrical Engineering and Computer Science, The University of Queensland, Brisbane, 4072, QLD, Australia*

Abstract

This paper addresses the challenge of human-guided navigation for mobile collaborative robots under simultaneous proximity regulation and safety constraints. We introduce Adaptive Reinforcement and Model Predictive Control Switching (ARMS), a hybrid learning–control framework that integrates a reinforcement learning (RL) follower trained with Proximal Policy Optimization (PPO) and an analytical one-step Model Predictive Control (MPC) formulated quadratic program (QP) safety filter. To enable robust perception under partial observability and non-stationary human motion, ARMS employs a decoupled sensing architecture with a Long Short-Term Memory (LSTM) temporal encoder for the human–robot relative state and a spatial encoder for 360° Light Detection and Ranging (LiDAR) scans. The core contribution is a learned adaptive neural switcher that performs context-aware soft action fusion between the two controllers, favoring conservative, constraint-aware QP-based control in low-risk regions while progressively shifting control au-

*Corresponding author

Email addresses: ning.liu@research.uwa.edu.au (Ning Liu),
senshen@link.cuhk.edu.hk (Sen Shen), zheng.li@research.uwa.edu.au (Zheng Li),
m.dsouza@uq.edu.au (Matthew D’Souza), jenjen.chung@uq.edu.au (Jen Jen Chung),
thomas.braunl@uwa.edu.au (Thomas Bräunl)

thority to the learned follower in highly cluttered or constrained scenarios where maneuverability is critical, and reverting to the follower action when the QP becomes infeasible to maintain continuous operation. Extensive evaluations against Pure Pursuit, Dynamic Window Approach (DWA), and an RL-only baseline demonstrate that ARMS achieves an 82.5% success rate in highly cluttered environments, outperforming DWA and RL-only approaches by 7.1% and 3.1%, respectively, while reducing average computational latency by 33% to 5.2 ms compared to a standalone multi-step MPC baseline. Additional sim-to-sim transfer in Gazebo and initial real-world deployment results further indicate the practicality and robustness of ARMS for safe and efficient human–robot collaboration. The source code and a demonstration video are publicly available at <https://github.com/21ning/ARMS.git>.

Keywords: Reinforcement learning, hybrid control, human–robot collaboration, adaptive switching, safety filtering, mobile robot navigation

1. Introduction

Mobile collaborative robots (cobots) are increasingly deployed to operate alongside humans in dynamic environments such as warehouses, hospitals, and laboratories. In these shared spaces, cobots must maintain a delicate balance by remaining sufficiently close to a human teammate to provide timely assistance while ensuring safe, collision-free operation in the presence of obstacles and other agents [1, 2]. In many practical settings, the robot is human-guided, where the human implicitly provides high-level intent through their motion, and the robot is responsible for executing local navigation in real time [3]. This coupling introduces a fundamental tension between proximity maintenance and safety, which becomes especially pronounced in cluttered environments with narrow passages and non-stationary human trajectories.

As illustrated in Fig. 1, achieving reliable human-guided navigation under these coupled constraints poses several challenges. First, the robot must react to dynamic hazards under partial observability while avoiding oscillatory or myopic behaviors in confined spaces [4]. Second, the proximity objective requires tracking a human trajectory whose future evolution is uncertain, where overly conservative motion may lead to loss of contact whereas aggressive behavior increases the risk of safety violations [5]. These difficulties are further exacerbated by strict real-time constraints on embedded hardware, which limit the applicability of computationally intensive multi-step optimization



Figure 1: Human-guided collaborative transport. The cobot executes real-time local navigation while carrying a payload, and the human provides high-level intent through motion. Proximity and safety constraints must be satisfied simultaneously in shared workspaces.

methods.

Classical local planners such as Dynamic Window Approach (DWA) and Model Predictive Control (MPC) provide predictable behavior and strong inductive biases through explicit modeling and constraint handling. However, in highly cluttered or narrow environments, these methods may become overly conservative or even infeasible when hand-designed cost functions fail to capture complex interaction dynamics [6]. In contrast, model-free reinforcement learning (RL) approaches can leverage experience to navigate diverse scenarios and adapt to complex geometries [7, 8]. Despite their flexibility, standard RL policies often lack explicit constraint handling and can exhibit unpredictable behavior near critical hazards [9, 10].

To address these limitations, we propose Adaptive Reinforcement and Model Predictive Control Switching (ARMS), a hybrid learning–control framework that combines the complementary strengths of analytical optimization and deep reinforcement learning (DRL) for human-guided mobile navigation. ARMS integrates a Proximal Policy Optimization (PPO) trained follower policy, capable of exploiting temporal context and learned heuristics, with an analytical one-step MPC-formulated quadratic program (QP) safety filter with horizon $H = 1$ that provides explicit, constraint-aware control when feasible. To support robust decision-making, ARMS employs a decoupled perception architecture in which a Long Short-Term Memory (LSTM) temporal encoder captures the human teammate’s relative motion state including relative position and velocity, while a spatial encoder processes 360° Light Detection and Ranging (LiDAR) scans for local environmental awareness.

The key innovation of ARMS lies in a learned adaptive neural switcher that performs soft, context-aware arbitration between the two controllers. Rather than viewing the safety filter as a last-resort intervention, the switcher is deliberately designed to favor conservative, QP-based control in low-risk regions with sufficient clearance, where predictable constraint-aware behavior is desirable. As environmental complexity increases and available clearance diminishes, control authority is progressively shifted toward the learned follower, whose experience-driven policy offers greater maneuverability in narrow, cluttered, or rapidly changing scenarios where optimization-based methods may become overly restrictive or infeasible. This asymmetric control allocation enables smooth transitions between analytical safety enforcement and agile learned behavior without chattering or hard switching.

The main contributions of this work are summarized as follows:

- A hybrid learning–control navigation framework named ARMS that integrates human-guided intent following with analytical safety filtering for mobile collaborative robots.
- A learned adaptive neural switcher that performs context-aware soft action fusion, favoring conservative QP-based control in low-risk regions and agile behavior of the learned follower in highly constrained environments.
- A decoupled perception design that combines LSTM-based temporal encoding of human motion with spatial encoding of LiDAR scans to handle heterogeneous interactive and geometric information.
- Extensive empirical evaluation demonstrating that ARMS achieves an 82.5% success rate in highly cluttered environments, outperforming classical and learning-based baselines while maintaining a high-frequency control rate.

2. Related Work

2.1. Human-Aware Mobile Robotics and Intent-Guided Navigation

Human–robot collaboration (HRC) in unstructured environments demands a seamless integration of safety, efficiency, and mutual predictability [11]. While foundational research has addressed task allocation and safety-aware scheduling for stationary manipulators [12, 13], human-guided mobile

navigation introduces non-stationary constraints in which the agent must maintain proximity to a moving teammate while negotiating dynamic clutter [14]. Recent advancements increasingly leverage deep representation learning to enhance robustness against occlusions and stochastic human trajectories [15, 16].

Effective human-aware navigation extends beyond simple following behavior and requires modeling complex social latent spaces, such as personal space and group cohesion [17]. Beyond traditional costmap extensions, modern approaches utilize Graph Neural Networks (GNNs) and socially aware cost maps to capture the topological dependencies between agents in dynamic scenes [18]. Furthermore, the availability of large-scale demonstration datasets [19] and standardized benchmarking platforms [20] has accelerated the development of imitation learning and generative models for capturing nuanced social cues in high-density environments.

2.2. *Classical Control and Constrained Optimization in Navigation*

Traditional navigation paradigms typically decompose the problem into global topological planning and local reactive control. Sampling-based planners, such as RRT*, are effective for static obstacle avoidance but often exhibit high computational variance in dynamic settings [21]. For local motion generation, velocity-space planners like the DWA remain industry standards due to their computational efficiency; however, they are frequently hindered by myopic decision-making and jerky trajectories in interactive crowd scenarios. Recent studies have sought to alleviate these limitations by incorporating trajectory smoothing constraints and socially aware interaction models into the local planning loop [22, 23].

Optimization-based frameworks, particularly MPC, provide a mathematically rigorous approach to constraint-aware motion generation. Social-force-model-based planners have been successfully employed to quantify human comfort as differentiable cost functions [24]. More recently, uncertainty-aware formulations have integrated probabilistic human motion prediction into constrained optimization frameworks to address the inherent stochasticity of pedestrian behavior [25]. Nevertheless, classical optimization methods remain susceptible to the freezing robot phenomenon in dense crowds, motivating the development of specialized collision-avoidance strategies that balance safety with goal-directed progress [26, 27].

2.3. Hybrid Learning-Control and Safety-Critical Reinforcement Learning

RL has emerged as a powerful paradigm for adaptive navigation, enabling the synthesis of complex control policies directly from interaction data. While early value-based approaches encountered scalability limitations, modern actor-critic architectures such as PPO and DDPG provide robust solutions for continuous control in high-dimensional state spaces [28, 29]. In human-centric navigation tasks, DRL demonstrates strong capabilities in encoding spatiotemporal reasoning and group dynamics, often reducing human discomfort compared to rigid rule-based systems [30, 31]. To address partial observability, memory-driven RL architectures, including LSTM-based policies, exploit temporal context to infer latent environmental dynamics [32].

Despite its flexibility, model-free RL lacks formal safety guarantees, which constitutes a major obstacle for deployment in real-world systems. This limitation has motivated the development of safety filters and shielding mechanisms that project RL-generated actions onto a safe and feasible control manifold [33, 34]. While previous work has primarily explored hard-switching shields, recent research suggests that soft fusion of learned heuristics and analytical filters can better preserve navigation fluidity [35], mirroring advancements in hybrid cooperative planning architectures for complex environments [36]. The ARMS framework extends this lineage by introducing a learned adaptive arbitration mechanism that utilizes risk-aware neural gating to dynamically balance the intuitive guidance of DRL with the rigorous safety guarantees of MPC-based filtering, specifically optimized for the non-stationary nature of human-guided transport.

3. Methods

3.1. Task Formulation and System Overview

A mobile robot navigates in a planar cluttered workspace $\mathcal{W} \subset \mathbb{R}^2$ containing static but initially unknown obstacles. The robot follows a human operator whose velocity varies over time and whose destination is not known a priori, introducing non-stationarity and stochasticity in the guidance signal. No global map is assumed; the robot relies solely on local 360° LiDAR and onboard odometry.

At each time step t , the robot observes a compact LiDAR representation together with the human-robot relative state. The control objective is human following under safety and collaboration constraints: (i) collisions

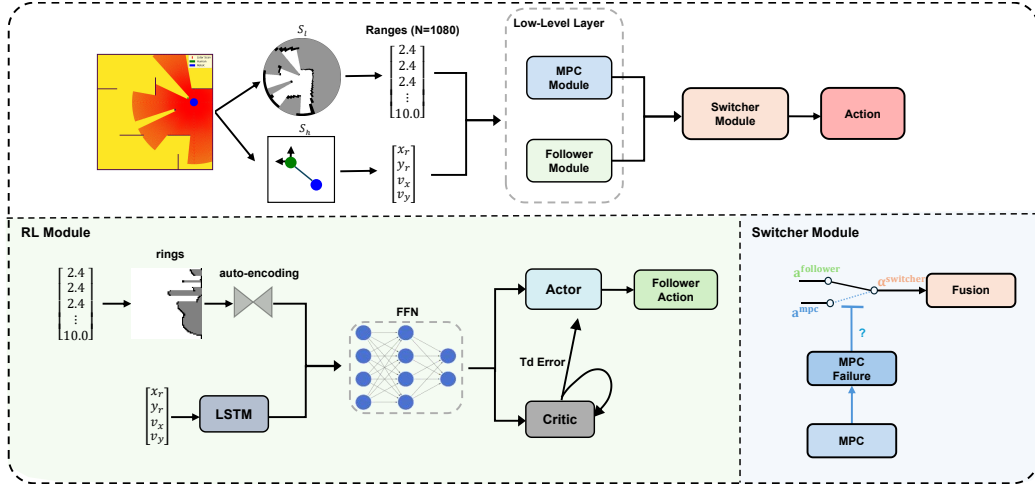


Figure 2: Overview of the proposed ARMS framework. A learned follower (trained via PPO) and a one-step MPC-formulated safety filter independently generate velocity commands from heterogeneous sensory inputs. A learned switcher observes compact risk features and softly fuses the two actions using an EMA-smoothed gating signal. When the safety QP is infeasible, execution falls back to the follower action.

with obstacles and the human are avoided, and (ii) the human–robot distance d_t^h is regulated within a comfort band $d_{\min}^{\text{conf}} < d_t^h < d_{\max}^{\text{conf}}$.

To balance tracking performance and safety in cluttered or narrow environments, we adopt a two-module architecture consisting of a learned low-level follower (trained via reinforcement learning) and an analytical one-step MPC-formulated safety filter. A learned switcher softly blends their outputs online based on compact risk-related features. The safety filter operates with a single-step horizon ($H = 1$) and provides conservative, constraint-aware control when feasible, while longer-term intent and maneuverability are primarily supplied by the learned follower.

In simulation, diverse operator trajectories are generated by sampling start–goal pairs on a 2D occupancy grid and computing shortest paths using A* with a Euclidean heuristic [37].

3.2. State Representation and Observation Design

The observation design targets human-guided navigation under partial observability and non-stationary human motion. Heterogeneous sensing modalities are explicitly separated into environment geometry and human motion cues.

3.2.1. LiDAR Encoding

We explicitly utilize a planar 2D LiDAR configuration in this work. While 3D LiDARs provide richer vertical information, planar LiDARs remain widely adopted in indoor mobile robots and warehouse AGVs due to their cost-effectiveness, lower data bandwidth, and reduced computational requirements. Such configurations are also commonly used in real-world autonomous systems operating under resource and latency constraints [38, 39]. This design choice is consistent with the objective of the ARMS framework, which aims to enable lightweight and high-frequency control suitable for deployment on resource-constrained embedded hardware.

Each 360° planar LiDAR scan with $N = 1080$ beams is projected to a 64×64 polar occupancy image. Following NavRep [40], the image is encoded using a pretrained convolutional VAE into a compact latent vector

$$\mathbf{z}_t \in \mathbb{R}^{32}, \quad (1)$$

which reduces input dimensionality and inference latency.

3.2.2. Temporal Encoding of Human Motion

In our simulation training environment, the human-robot relative state s_t^h is derived directly from the physics engine to isolate the control policy's performance from perception noise. However, the ARMS architecture is designed to be agnostic to the source of this state. For real-world deployment, s_t^h is estimated via an onboard RGB-D perception pipeline, where the LSTM encoder serves not only to model temporal dependencies but also to smooth noisy detection measurements and infer human motion intent.

To capture the non-stationary nature of human guidance, temporal aggregation is applied to the human–robot relative state rather than the LiDAR representation. Let the relative position and velocity in the robot frame be

$$\mathbf{p}_t^h = \begin{bmatrix} \Delta x_t \\ \Delta y_t \end{bmatrix}, \quad \mathbf{v}_t^h = \begin{bmatrix} v_{x,t}^h \\ v_{y,t}^h \end{bmatrix}. \quad (2)$$

The human motion state is defined as $\mathbf{s}_t^h = [\mathbf{p}_t^h, \mathbf{v}_t^h]$. A lightweight single-layer LSTM with hidden size $H_{\text{LSTM}} = 64$ aggregates a short history to filter observation noise and capture the latent non-stationary intent of the human teammate:

$$\mathbf{h}_t^h = \text{LSTM}(\mathbf{s}_{t-K+1:t}^h). \quad (3)$$

At episode start, the history buffer is warm-started by repeating the earliest available state. Observations and actions are updated at 20 Hz.

Reward Term	Expression
Survival Increment	+0.01
Termination Penalty	-8
Proximity Regulation	$0.5 - \min(d - 1.1 , 0.5)$
Comfort Zone Reward	$+0.1 \cdot \mathbb{I}[0.9 \leq d \leq 1.3]$
Quadratic Clearance Penalty	$-0.5 \cdot \max(0.5 - c, 0)^2$
Clearance Incentive	$+0.05 \cdot \min(c - 1.0, 1.0) \cdot \mathbb{I}[c \geq 1.0]$
Critical Safety Penalty	$-6.0 \cdot \max(0.2 - c, 0)$
Pre-collision Warning	$-1.5 \cdot \max(0.10 - c, 0)$
Drift Penalty	$-0.2 \cdot t_{\text{far}}$

Table 1: Follower environment reward components r_{env} .

3.2.3. Follower Observation

The learned follower receives a dictionary observation

$$\mathcal{O}_t^{\text{f}} = \{\mathbf{z}_t, \mathbf{h}_t^h, c_t, \mathbf{v}_t^c\}, \quad (4)$$

where c_t denotes the minimum LiDAR clearance and \mathbf{v}_t^c the associated direction toward the closest obstacle proxy. All observation components are normalized using running statistics.

3.2.4. Switcher Observation

The adaptive switcher does not access the full observation. Instead, it receives a compact risk feature vector ϕ_t defined in Sec. 3.3.5.

3.3. ARMS Hybrid Control

3.3.1. Follower Policy and Action Space

The follower policy outputs omnidirectional velocity commands $\mathbf{a}_t^{\text{f}} = [v_x, v_y] \in \mathbb{R}^2$, bounded by platform-specific velocity and acceleration limits. The actor produces a Gaussian distribution during training and executes the mean action during deployment.

3.3.2. Reward Design

The human–robot distance is $d_t = \|\mathbf{p}_t^h\|_2$, and the minimum obstacle clearance is $c_t = \min(\text{scant}_t)$. The follower is trained using environment rewards summarized in Table 1. Additional shaping terms for training the switcher are summarized in Table 2.

Reward Component	Expression
Base Environment Reward	r_{env}
Safety-filter Utilization Bias	$-\lambda(1 - \bar{\alpha})$
Clearance-aware Modulation	$\beta \bar{\alpha}[1 - 2\sigma(k(\tau - c))]$

Table 2: Switcher reward shaping terms

3.3.3. Policy Optimization

The follower policy π_{θ}^f is optimized via reinforcement learning using PPO with a MultiInputPolicy. All modalities are concatenated internally and processed by an MLP with hidden layers 256–256–128. Generalized Advantage Estimation is used with $\gamma = 0.94$ and $\lambda_{\text{GAE}} = 0.92$.

3.3.4. One-step MPC-formulated QP Safety Filter

We denote the MPC horizon length as H ; the proposed QP safety filter corresponds to the one-step case ($H = 1$), while the MPC baseline uses a longer horizon ($H = 10$).

We solve a one-step convex QP to generate a conservative, constraint-aware velocity command. Let $\mathbf{u}_t \in \mathbb{R}^2$ denote the QP decision variable. Assuming the human velocity \mathbf{v}_t^h is locally constant within Δt , the relative position evolves as

$$\mathbf{p}_{t+1}^h = \mathbf{p}_t^h + (\mathbf{v}_t^h - \mathbf{u}_t)\Delta t. \quad (5)$$

We define a reference relative position $\mathbf{p}_t^{h,\text{ref}} = d_{\text{ref}} \frac{\mathbf{p}_t^h}{\|\mathbf{p}_t^h\|_2 + \epsilon}$ and solve

$$\begin{aligned} \mathbf{u}_t^* = \arg \min_{\mathbf{u}_t \in \mathbb{R}^2} & \left\| \mathbf{p}_t^h + (\mathbf{v}_t^h - \mathbf{u}_t)\Delta t - \mathbf{p}_t^{h,\text{ref}} \right\|_2^2 + \rho \|\mathbf{u}_t - \mathbf{a}_{t-1}\|_2^2 \\ \text{s.t. } & \mathbf{u}_{\min} \leq \mathbf{u}_t \leq \mathbf{u}_{\max}, \\ & |\mathbf{u}_t - \mathbf{a}_{t-1}| \leq a_{\max} \Delta t, \\ & \mathbf{n}_{i,t}^\top \mathbf{u}_t \leq \frac{r_{i,t} - c_{\text{safe}}}{\Delta t}, \quad i \in \mathcal{I}_t. \end{aligned} \quad (6)$$

The objective consists of a one-step tracking term and a smoothness regularizer. The first term penalizes the predicted deviation of the next-step relative position from a desired reference at distance d_{ref} along the current bearing to the human, encouraging the robot to maintain the comfort-band center while following the operator. The second term discourages large

deviations from the previously executed command \mathbf{a}_{t-1} , promoting smooth velocities across switching and mitigating oscillatory behaviors. The box constraint $\mathbf{u}_{\min} \leq \mathbf{u}_t \leq \mathbf{u}_{\max}$ enforces actuator-level velocity limits, while the rate constraint $|\mathbf{u}_t - \mathbf{a}_{t-1}| \leq a_{\max} \Delta t$ approximates acceleration bounds under a discrete-time command interface. Finally, the linearized inequality constraints enforce one-step clearance with respect to selected LiDAR rays or obstacle proxies, yielding conservative, constraint-aware corrections when the QP is feasible.

We denote the safety-filter output by $\mathbf{a}_t^{\text{QP}} := \mathbf{u}_t^*$. Here, $(r_{i,t}, \theta_{i,t})$ denote the range and bearing of selected LiDAR rays (or obstacle proxies) \mathcal{I}_t , and $\mathbf{n}_{i,t} = [\cos \theta_{i,t}, \sin \theta_{i,t}]^\top$. The linear inequality enforces a one-step linearized clearance constraint $r_{i,t+1} \gtrsim r_{i,t} - \Delta t \mathbf{n}_{i,t}^\top \mathbf{u}_t \geq c_{\text{safe}}$. We set $\text{valid}_t = 1$ if the solver returns a feasible solution within the time limit; otherwise $\text{valid}_t = 0$.

When the QP becomes infeasible, this typically indicates that the conservative one-step linearized constraints collapse the feasible set in narrow passages, rather than the absence of a physically admissible motion. In such cases, ARMS falls back to the learned follower to avoid freezing. Importantly, the executed command remains subject to the same actuator bounds, which preserves continuous and bounded operation even when the QP fails.

3.3.5. Adaptive Switching via Soft Gating

At each step, the switcher observes a compact risk feature vector

$$\phi_t = [c_t, \text{ttc}_{\min,t}, j_t, e_t^d, \text{valid}_t], \quad (7)$$

where c_t is the minimum LiDAR clearance, $\text{ttc}_{\min,t}$ is the minimum time-to-collision estimate from LiDAR rays, j_t is a smoothness surrogate defined as $j_t = \|a_{t-1} - a_{t-2}\|_2 / \Delta t$, and $e_t^d = |d_t - d_{\text{ref}}|$ is the human-following band tracking error with $d_t = \|p_t^h\|_2$ and $d_{\text{ref}} = (d_{\min}^{\text{comf}} + d_{\max}^{\text{comf}})/2$. $\text{valid}_t \in \{0, 1\}$ indicates whether the QP solver returns a feasible solution.

The switcher policy outputs a gating signal $\alpha_t \in [0, 1]$, which is smoothed using an exponential moving average (EMA):

$$\bar{\alpha}_t = \eta \alpha_t + (1 - \eta) \bar{\alpha}_{t-1}. \quad (8)$$

Both during training and deployment, action fusion is performed using $\bar{\alpha}_t$:

$$\mathbf{a}_t = (1 - \bar{\alpha}_t) \mathbf{a}_t^{\text{f}} + \bar{\alpha}_t \mathbf{a}_t^{\text{QP}}. \quad (9)$$

The switcher is trained with PPO using the augmented reward

$$r_t^{\text{sw}} = r_t^{\text{env}} + \mathbb{I}[\text{valid}_t] \left(-\lambda(1 - \bar{\alpha}_t) + \beta \bar{\alpha}_t (1 - 2\sigma(k(\tau - c_t))) \right), \quad (10)$$

where $\lambda = 0.08$, $\beta = 0.3$, $\tau = 0.5$, $k = 8$, and $\sigma(x) = (1 + e^{-x})^{-1}$. When $\text{valid}_t = 0$, all $\bar{\alpha}_t$ -dependent shaping terms are disabled to align the training signal with the executed control.

Both the follower policy and the QP module output velocity commands in the same bounded action space. Therefore, the executed command after fusion in Eq. 9 (followed by clipping) always satisfies the actuator-level velocity limits. However, obstacle clearance constraints are state-dependent and are only enforced when the QP is feasible. Hence, we do not claim a formal safety guarantee under all conditions; instead, the QP module serves as a conservative, constraint-aware corrective controller that empirically reduces collision risk when feasible.

This switching strategy reflects an explicit asymmetry in control roles. In low-risk regions with sufficient clearance, the switcher biases control toward the QP safety filter, yielding conservative and predictable constraint-aware behavior. As environmental complexity increases and clearance diminishes, control authority is progressively shifted toward the learned follower, whose experience-driven policy provides greater maneuverability in narrow or highly constrained environments where optimization-based methods may become overly restrictive or infeasible.

It is worth noting that QP infeasibility in cluttered environments typically arises from the conservatism of linearized safety constraints within non-convex geometries, rather than the physical absence of a valid path. In such “deadlock” scenarios, the learned follower—having been trained with collision penalties across diverse fragmented spaces—provides essential maneuverable behaviors. It can navigate through tight gaps where the rigid, linearized constraints of the MPC would otherwise cause the robot to freeze or fail to find a feasible solution. By adaptively shifting the weight toward the RL-based follower, ARMS maintains mission-level progress while ensuring the robot does not become trapped by overly-conservative analytical bounds.

4. Experiments

4.1. Experimental Setup and Dataset Statistics

All experiments are conducted in a high-fidelity synthetic environment that follows the OpenAI Gym interface and is tailored for trajectory replay.

Algorithm 1: ARMS Soft Action Fusion

Input: Follower observation \mathcal{O}_t^f ;
 Base observation $\mathcal{O}_t^{\text{base}}$;
 Previous gate $\bar{\alpha}_{t-1}$;
 Previous executed actions $\mathbf{a}_{t-1}, \mathbf{a}_{t-2}$;
 Follower policy π_θ^f ;
 Switcher policy π_φ^s ;
 QP safety solver

Output: Executed action \mathbf{a}_t

$$\begin{aligned}
 \mathbf{a}_t^f &\leftarrow \pi_\theta^f(\mathcal{O}_t^f); \\
 (\mathbf{a}_t^{\text{QP}}, \text{valid}_t, A_t, b_t) &\leftarrow \text{SOLVESAFETYQP}(\mathcal{O}_t^{\text{base}}, \mathbf{a}_{t-1}); \\
 \text{if } \neg \text{valid}_t \text{ then} \\
 &\quad \mathbf{a}_t^{\text{QP}} \leftarrow \mathbf{a}_t^f; \\
 (c_t, \text{ttc}_{\min, t}) &\leftarrow \text{COMPUTECLEARANCETTC}(\mathcal{O}_t^{\text{base}}); \\
 d_t &\leftarrow \text{HUMANDISTANCE}(\mathcal{O}_t^{\text{base}}); \\
 e_t^d &\leftarrow |d_t - d_{\text{ref}}|; \\
 j_t &\leftarrow \|\mathbf{a}_{t-1} - \mathbf{a}_{t-2}\|_2 / \Delta t; \\
 \phi_t &\leftarrow [c_t, \text{ttc}_{\min, t}, j_t, e_t^d, \text{valid}_t]; \\
 \alpha_t &\leftarrow \pi_\varphi^s(\phi_t); \\
 \bar{\alpha}_t &\leftarrow \eta \alpha_t + (1 - \eta) \bar{\alpha}_{t-1}; \\
 \text{if } \text{valid}_t \text{ and } \text{VIOLATES}(A_t, b_t, \mathbf{a}_t^f) \text{ then} \\
 &\quad \bar{\alpha}_t \leftarrow 1; \\
 \mathbf{a}_t &\leftarrow (1 - \bar{\alpha}_t) \mathbf{a}_t^f + \bar{\alpha}_t \mathbf{a}_t^{\text{QP}}; \\
 \mathbf{a}_t &\leftarrow \text{CLIP}(\mathbf{a}_t); \\
 \mathbf{a}_t &\leftarrow \text{RATELIMIT}(\mathbf{a}_t, \mathbf{a}_{t-1}); \\
 \text{return } \mathbf{a}_t;
 \end{aligned}$$

To evaluate generalization under non-stationary human guidance, we curate a large-scale dataset of human reference trajectories, comprising 5,000 training and 5,000 testing episodes. The mean episode length is 279.77 steps for training and 241.96 steps for testing, with a control interval of $\Delta t = 0.05$ s.

Human motion statistics are closely matched across splits: speeds range from standstill to approximately 0.54 m/s, with an average around 0.32 m/s (including stop-and-go segments). To guarantee task feasibility and ensure a fair evaluation, reference trajectories are generated by an A^* planner on the map-specific occupancy grid, ensuring that all paths are physically traversable. This design isolates the navigation task as a direct evaluation of the policy's sensorimotor intelligence rather than global path feasibility.

The robot is modeled as a planar omnidirectional base. It is controlled

at a frequency of 20 Hz ($\Delta t = 0.05$ s) via a continuous action space that includes both 2D velocity $\mathbf{v}_t = [v_x, v_y] \in [-1, 1]^2$ m/s and 2D acceleration $\mathbf{a}_t = [a_x, a_y] \in [-1, 1]^2$ m/s². Episodes terminate under four conditions: (i) collision ($c_t \leq 0$), (ii) violation of personal space ($d_t < 0.5$ m), (iii) timeout due to excessive separation ($d_t > 2.5$ m for 20 consecutive steps), or (iv) successful trajectory completion.

4.2. Feature Processing and Sensory Modules

We employ a decoupled sensing architecture to mitigate the high-dimensional complexity of environmental geometries.

A pre-trained spatial encoder compresses the LiDAR manifold into a 32-D latent space \mathbf{z}_t , facilitating representation stability. This embedding captures local geometric structures in a compact representation. Consistent with our design philosophy, LiDAR observations are treated as instantaneous spatial inputs without temporal aggregation.

Conversely, temporal modeling is dedicated exclusively to human motion cues. The relative position and velocity between the human and robot are aggregated over a short history using a lightweight LSTM encoder. This produces a 64-dimensional human motion feature \mathbf{h}_t^h , designed to capture non-stationary guidance behaviors.

The resultant observation vector comprises the LiDAR latent \mathbf{z}_t , the human motion embedding \mathbf{h}_t^h , the minimum obstacle clearance c_t , and the direction vector toward the nearest obstacle. To ensure representation stability, all encoding modules remain frozen during the reinforcement learning phase.

4.3. Training Protocol

Training Curriculum. We implement a hierarchical two-stage curriculum that decouples low-level reactive locomotion from high-level control arbitration. This separation allows the system to first master collision avoidance before learning when to deploy it. The specific PPO hyperparameters for both stages are contrasted in Table 3.

4.3.1. Stage 1: Follower Pre-training

We pre-train the learned Follower policy π_θ^f to acquire reactive, short-horizon collision avoidance behaviors. We select *Scenario 2: Boundary-Constrained Passage* for this stage, as its dense obstacle distribution and corridor constraints provide an informative learning signal for safety-critical reactions. To bias learning toward immediate clearance in cluttered spaces,

we use a larger-capacity network for the Follower and a smaller discount factor (γ), encouraging near-term obstacle avoidance over long-horizon path optimality.

4.3.2. Stage 2: Switcher Optimization

With the Follower parameters frozen, we train the Switcher policy π_φ^s to learn arbitration in *Scenario 3: Fragmented Narrow-Space*, whose fragmented topology requires frequent shifts between tracking-driven commands and conservative, constraint-aware corrections.

Unlike the Follower, the Switcher employs a higher discount factor to internalize the long-term implications of its fusion weight (α_t) assignments. To ensure real-time efficiency on embedded hardware, the Switcher adopts a compact MLP structure. During this stage, we incorporate EMA smoothing (Eqs. 8–9) and the reward shaping terms defined in Eq. 10 to stabilize the transitions between the two underlying controllers.

Implementation Details. The structural and parametric variances summarized in Table 3 are tailored to the distinct functional roles of each module:

- **Reactive Priority (Follower):** The Follower employs a high-capacity network and a reduced discount factor ($\gamma = 0.94$). This design encourages the agent to prioritize immediate, local geometric constraints over long-term cumulative rewards, which is essential for maintaining safety in the dense clutter of *Scenario 2*. The larger batch size further ensures gradient stability amidst high-frequency state transitions.
- **Strategic Arbitration (Switcher):** Conversely, the Switcher utilizes a streamlined architecture to minimize inference latency during high-level decision-making. By adopting a near-unity discount factor ($\gamma = 0.99$), the Switcher is incentivized to consider the long-term impact of its arbitration on human-robot collaboration stability. The smaller batch size facilitates rapid convergence during the fine-tuning phase on the pre-trained follower’s latent space.

4.4. Baselines and Metrics

We benchmark ARMS against the following baselines:

- **Pure Pursuit:** A geometric tracking baseline.
- **DWA:** A sampling-based local planner.

Table 3: PPO Hyperparameter Settings.

Category	MultiInputPolicy	MlpPolicy
<i>Policy Architecture</i>		
Policy Type	MultiInputPolicy	MlpPolicy
Network Architecture	[256, 256, 128]	[64, 64]
Activation Function	Tanh	Tanh
<i>Optimization</i>		
Learning Rate	Linear (1e-4 → 0)	Fixed (3e-4)
Batch Size	2048	256
n_{steps}	512	2048
n_{epochs}	10	10
Max Grad Norm	0.5	0.5
<i>RL Mechanics</i>		
Discount Factor (γ)	0.94	0.99
GAE Lambda (λ)	0.92	0.95
Clip Range	0.2	0.2
Normalize Advantage	True	True
Entropy Coef	0.0	0.0
Value Function Coef	0.5	0.5

- **Standalone Follower (RL):** The pre-trained RL follower without safety filtering.
- **MPC Baseline (H=10):** A traditional model predictive controller ($H = 10$) serving as a benchmark for safety and computational latency.
- **ARMS:** The work proposed hybrid system fusing PPO and a 1-step QP ($H = 1$).

Pure Pursuit. A fixed control period of 0.05 s (20 Hz) is employed, with a lookahead distance $d_{\text{des}} = 0.8$ m, maximum speed $v_{\text{max}} = 0.9$ m/s, and acceleration clipping at 0.5 m/s².

DWA. The DWA baseline is implemented as a simplified heuristic rather than a sampling-based method. This design choice avoids reliance on velocity sample counts or traditional clearance, progress, and heading weights. To ensure optimal performance, all hyperparameters were determined via a

systematic grid search on the training dataset, with search ranges summarized in Table 4.

Evaluation Metrics. To provide a multifaceted assessment of the navigation performance, we employ four key metrics:

- **Success Rate (SR):** The percentage of episodes in which the robot successfully completes the reference trajectory without collisions, personal space violations, or timeouts.
- **Human Distance (HD):** The mean separation distance between the robot and the human throughout an episode, reflecting the overall following performance.
- **Safe Distance (SD):** The average distance maintained to the human specifically when within a predefined interaction range, capturing safety-critical proximity behavior.
- **Average Runtime (RT):** The computational latency per control step.

The inclusion of RT is crucial for verifying the benefits of computational offloading. It quantifies how RL-based anticipation can effectively supplant computationally intensive multi-step optimization. By reducing the reliance on complex iterative solvers, our approach aims to mitigate solver latency spikes and ensure deterministic real-time control in embedded applications.

Table 4: Grid Search Ranges for DWA Hyperparameters.

Parameter	Search Range / Values
Max Velocity (v_{\max})	{0.6, 0.8, 1.0}
Acceleration (accel)	{0.4, 0.6, 0.8}
Desired Distance	{1.0, 1.2, 1.4}
Follow Gain	{0.6, 0.9, 1.2}
Avoid Gain	{1.0, 1.4, 1.8}
Avoid Clearance	{0.8, 1.0, 1.2}
Personal Space	{0.8, 0.9, 1.0}
Obstacle Buffer	{0.9, 1.0, 1.2}
Obstacle Free Clearance	{1.6, 1.8, 2.0}

Table 5: Performance comparison of different navigation methods across three scenarios in 2D world. Metrics: success rate (SR, \uparrow , %), average human distance (HD, \uparrow , m), average safe distance (SD, \uparrow , m), and average runtime per control step (Avg. RT, \downarrow , ms). All results are averaged over 300 trials

Method	Scenario 1			Scenario 2			Scenario 3			\downarrow Avg. RT (ms)
	\uparrow SR (%)	\uparrow HD	\uparrow SD	\uparrow SR (%)	\uparrow HD	\uparrow SD	\uparrow SR (%)	\uparrow HD	\uparrow SD	
Pure Pursuit	95.3	1.184	1.212	44.6	1.163	0.671	18.7	1.151	0.576	0.0126
DWA	96.2	1.028	1.094	86.5	1.043	0.809	75.4	1.061	0.639	0.0215
Follower	98.9	1.071	1.180	91.3	1.100	0.780	79.4	1.120	0.660	0.1460
MPC	98.4	1.125	1.215	53.1	1.270	0.860	24.1	1.240	0.700	7.8620
ARMS	99.1	1.115	1.205	93.7	1.240	0.840	82.5	1.230	0.690	5.240

5. Results

5.1. Main Benchmark Results

We evaluate the ARMS framework through a series of comparative simulations and ablation studies. The primary objective is to demonstrate that the hybrid architecture can maintain high navigation success rates in cluttered environments while significantly reducing computational latency through strategic offloading.

Table 5 reports a quantitative comparison between ARMS and representative baselines across three benchmark scenarios with progressively increasing geometric constraints. Overall, ARMS achieves better safety and efficiency—reflected in lower collision/personal-space violation rates and improved task completion performance—with the advantage becoming more pronounced as the environment becomes more cluttered.

Scenario 1: Obstacle-Free Corridor. An unobstructed corridor where obstacle-avoidance constraints are rarely active. The primary challenge is stable dynamic tracking of non-stationary guidance while remaining within the collaboration band.

Scenario 2: Boundary-Constrained Passage. Static obstacles are placed along corridor boundaries. Although a central passage typically exists, the controller must balance proximity maintenance against lateral clearance when reacting to deviations from the nominal trajectory.

Scenario 3: Fragmented Narrow-Space. Obstacles appear near the human and along the reference path, resulting in narrow and fragmented free space. This scenario requires frequent local adjustments and stresses the tight coupling between proximity regulation and collision avoidance.

Across all baselines, performance consistently degrades as the geometric constraints tighten from Scenario 1 to Scenario 3, with the most pronounced

drop observed in the fragmented narrow-space setting (Scenario 3). This trend aligns with a higher prevalence of risk states—characterized by reduced clearance and shorter Time-to-Collision (TTC)—in which purely reactive control or overly conservative safety corrections can readily trigger failures (either collisions or out-of-range terminations), particularly in narrow passages with rapidly changing local geometry.

5.2. Main Benchmark Results

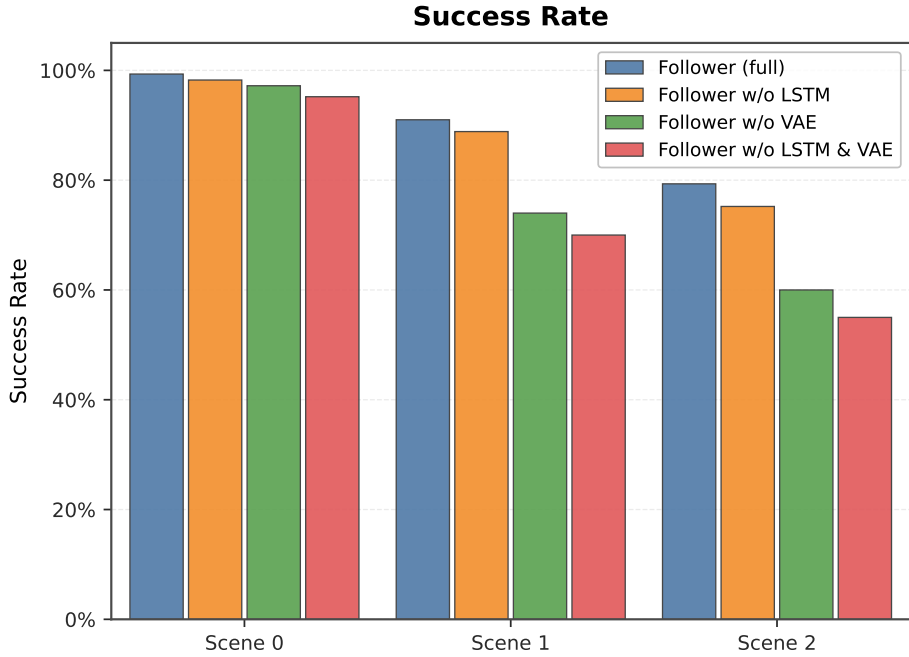
The proposed hybrid controller improves robustness in clutter by combining the agile sensorimotor response of the learned follower with a lightweight one-step QP safety filter. In terms of computational efficiency, ARMS achieves a 33% reduction in average latency compared to the standalone multi-step MPC baseline ($H = 10$). This acceleration stems from the switcher’s ability to selectively bypass iterative optimization spikes, offloading control to the RL follower when entering non-convex narrow passages. This speedup is achieved through two mechanisms: (i) *Horizon Reduction*: ARMS leverages the RL policy’s long-term anticipation to replace the computationally expensive multi-step optimization, requiring only a single-step safety check. (ii) *Computational Offloading*: In highly constrained regions where traditional solvers typically suffer from latency spikes due to exhaustive iterative searches, the learned switcher proactively identifies the QP’s potential infeasibility and offloads control authority to the learned follower. This bypasses redundant optimization attempts in non-convex regions, ensuring real-time performance even in the most difficult scenarios.

5.3. Ablation Studies

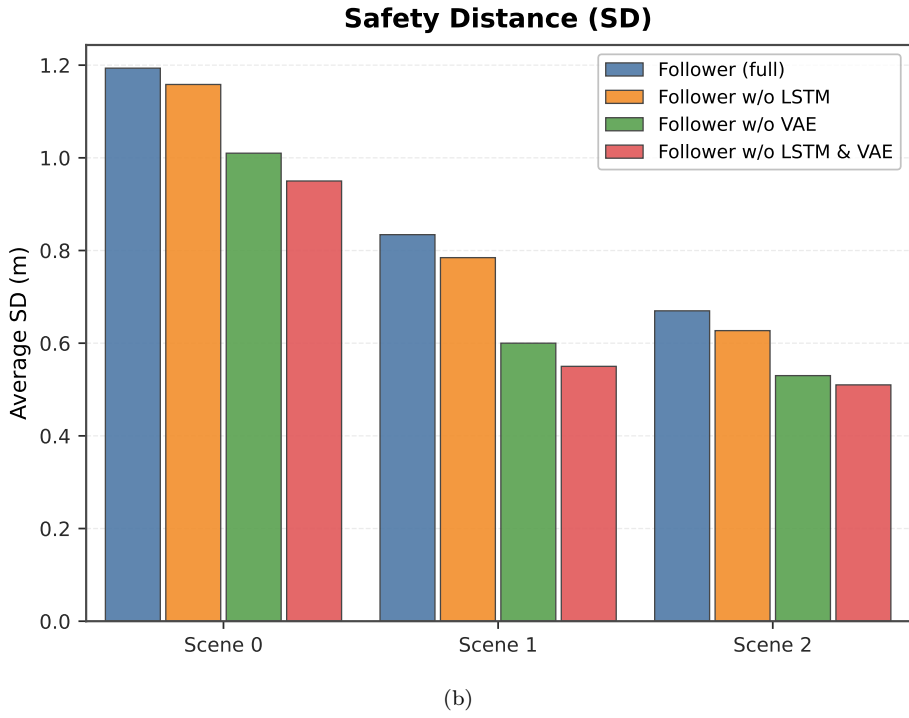
To systematically evaluate the architectural contributions of (i) the decoupled perception stream (comprising the LiDAR VAE and human-motion LSTM) and (ii) the risk-aware neural switcher, we conduct a series of ablation experiments. The performance trajectories are visualized in Fig. 3 and Fig. 4. To ensure a principled comparison, all architectural variants utilize identical reinforcement learning (PPO) hyperparameters and interaction budgets.

Ablation Definitions and Reproducibility. The PPO-based follower ablations maintain consistent reward formulations and switching mechanisms while selectively pruning the observation pipeline:

- **Follower-Full:** The baseline follower utilizing the complete latent representation $\{z_t, h_t^h, c_t, v_t^c\}$, where $z_t \in \mathbb{R}^{32}$ is the frozen spatial latent



(a)



(b)

Figure 3: Ablation analysis of Follower variants in Scenario 3, averaged over a total of 300 evaluation trials. (a) Success rate across 20 distinct navigation scenarios. (b) Average obstacle clearance maintained by the corresponding configurations.

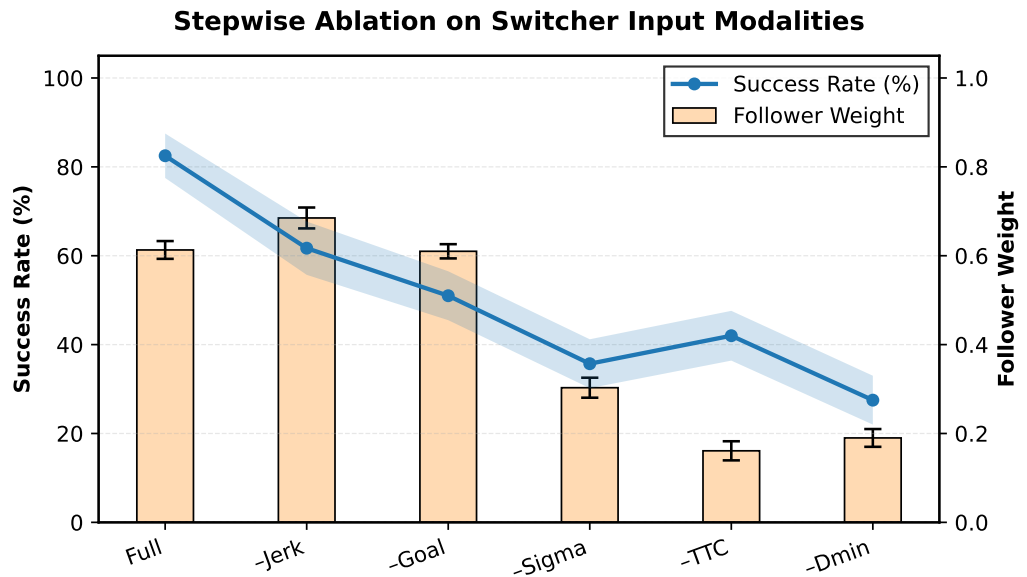


Figure 4: Comparative ablation of the switcher architecture in Scenario 3, illustrating the effect of feature selection and fusion strategies on navigation success. Results are averaged over a total of 300 evaluation trials, with shaded bands and error bars indicating the 95% confidence intervals.

from the LiDAR VAE and $h_t^h \in \mathbb{R}^{64}$ represents the temporal embedding from the LSTM.

- **Follower w/o LSTM:** The temporal encoder is bypassed, replacing h_t^h with the instantaneous human–robot relative state $s_t^h = [p_t^h, v_t^h]$. This variant tests the necessity of modeling temporal dependencies in non-stationary guidance.
- **Follower w/o VAE:** The pre-trained spatial encoder is removed. The policy receives a normalized raw LiDAR range vector $r_t \in \mathbb{R}^{1080}$, evaluating the efficiency of manifold learning over high-dimensional sensory input.
- **Follower w/o LSTM & VAE:** A model-free baseline using raw LiDAR ranges r_t and instantaneous state s_t^h , providing a lower-bound for the perception architecture’s impact.

Table 6: Comparison of switching strategies for combining Follower and MPC in Scenario 3. Metrics include SR, HD, SD, and MPC weight (MW). All results are averaged over a total of 300 evaluation trials.

Switching strategy	↑ SR (%)	↑ HD (m)	↑ SD (m)	MW
Logic-based Switcher	72.1	1.102	0.651	0.228
Distance-based Switcher	78.3	1.154	0.673	0.472
ARMS	82.5	1.230	0.690	0.387

Switcher ablations examine the high-level arbitration logic:

- **Full Switcher (Soft Fusion):** The proposed continuous weight predictor using features $\{d_{\min}, \text{ttc}_{\min}, \text{jerk}, \text{band_error}, \text{valid}\}$, mapping to $\alpha_t \in [0, 1]$ via EMA-smoothed soft fusion.
- **Feature Dropout:** Systematic removal of individual risk-aware features to quantify their sensitivity for arbitration; results are visualized in Fig. 4.
- **Hard Gating:** Replaces soft fusion with a deterministic binarized threshold τ (with hysteresis $\Delta\tau$), enforcing $\alpha_t \in \{0, 1\}$ when the QP solution is valid. Quantitative results are reported in Table 6.

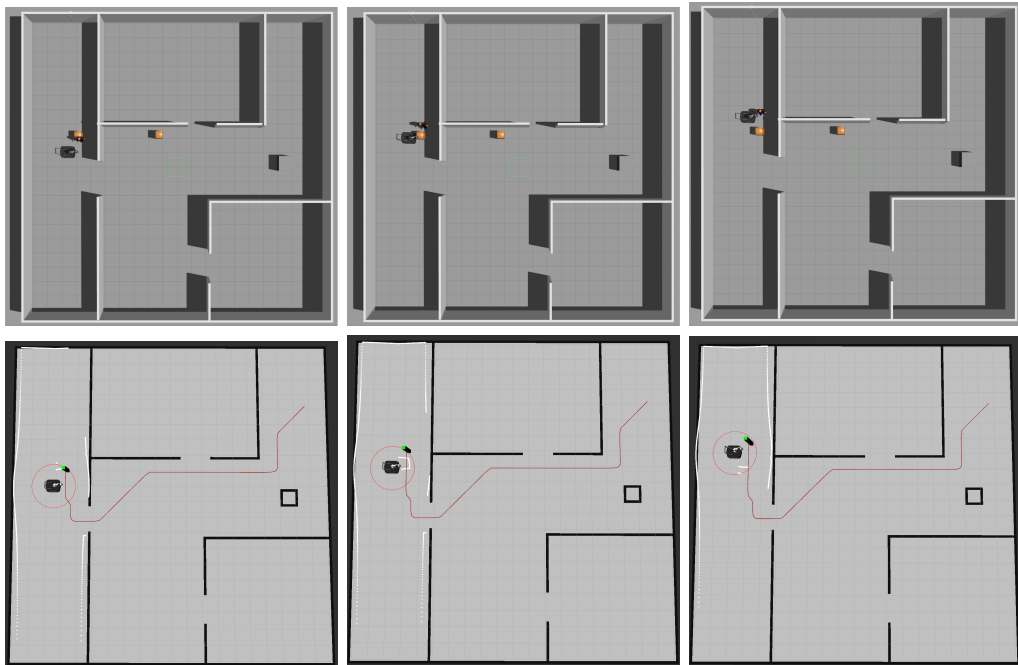


Figure 5: Representative Gazebo evaluation in a cluttered hallway. Two static obstacles are placed along the corridor while a human actor follows a goal-directed trajectory. The robot receives 2D LiDAR scans and outputs velocity commands. The bottom row shows the corresponding RViz visualizations: the red circle denotes the desired following region around the operator, and the red curve indicates the operator trajectory. The robot stays within the following region while maneuvering around obstacles and maintaining a safe separation distance.

Perception Module Analysis. This ablation quantifies the efficacy of decoupled neural representations in stabilizing the follower’s policy. The Follower-Full model leverages both compressed spatial geometry and temporal intent embeddings. As illustrated in Fig. 3, the degradation of the SR is most pronounced when both encoders are omitted.

The removal of the **LiDAR VAE** necessitates that the policy learns control heuristics directly from high-dimensional, redundant range data. This increases sample complexity and impairs the model’s ability to extract robust geometric abstractions, leading to significantly lower obstacle clearance in novel, cluttered environments. Conversely, removing the **human-motion LSTM** restricts the agent to a purely Markovian observation of relative state. This eliminates the capacity for intent inference, resulting in reactive and oscillatory steering behaviors when the operator exhibits non-linear movement, thereby compromising safety under constrained clearances.

Switcher Design and Risk-Aware Arbitration. The arbitration logic’s robustness is evaluated through structural modifications to the switcher. As shown in Fig. 4, omitting risk-sensitive surrogates, particularly Time-to-Collision (TTC) or the minimum clearance (c_t), leads to a marked decrease in robustness within dense obstacle fields. This indicates that the switcher relies primarily on immediate collision-risk cues rather than secondary tracking errors when allocating control authority. In addition, Table 6 contrasts soft fusion with hard gating. The results suggest that binary switching tends to induce command chattering near decision boundaries, which can degrade mechanical stability and human comfort. In contrast, soft fusion enables a smoother transfer of authority, which is essential for stable navigation under frequent transitions between the learned follower and the QP-based safety filter.

5.4. Gazebo Evaluation and Deployment Discussion

We emphasize that the Gazebo evaluation is intended as a qualitative sim-to-sim validation of the arbitration behavior, rather than a quantitative benchmark.

To evaluate the robustness of the ARMS framework in a physically realistic environment, we deployed the trained policies into the Gazebo simulator. Unlike the trajectory-replay Gym environment, Gazebo provides a full ROS-based stack with realistic dynamics and asynchronous sensor timing, serving



Figure 6: Real-world indoor deployment of the proposed system. The robot estimates the operator’s position from onboard camera observations and successfully follows the operator along an entire trajectory while safely avoiding obstacles.

as a critical sim-to-sim testbed for bridging the gap between algorithmic design and hardware deployment.

In our setup, we utilized a Clearpath Ridgeback omnidirectional platform equipped with a 360° planar LiDAR. Moving from the idealized Gym environment to Gazebo introduces several physical challenges, including rigid-body physics, measurement noise ($\sigma_r = 0.02$ m), and actuation latency. Velocity commands are executed at 20 Hz within the ROS pipeline. To capture the delays inherent in ROS transport, we modeled an end-to-end latency of 1–2 control ticks. These constraints test the policy’s ability to maintain stability when sensor updates and control cycles are not perfectly synchronized.

The Gazebo evaluation focuses on a qualitative behavior analysis of the switcher’s arbitration logic. As illustrated in Fig. 5, the robot must follow a human actor through a hallway cluttered with static obstacles. Our observations reveal that the learned switcher effectively manages control authority: in open areas, the system favors the QP filter for its precise safety guarantees; however, when entering narrow passages where the QP’s feasible region shrinks, the switcher proactively reallocates weight to the RL follower. This transition prevents the freezing robot problem—where traditional

optimization-based methods often stall due to conservative constraints or solver infeasibility—enabling more fluid and continuous maneuvers.

Furthermore, we conducted preliminary indoor experiments using the same ROS stack and the learned policy without any retraining. As shown in Fig. 6, qualitative results indicate that the proposed risk-conditioned switcher effectively handles real-world sensor noise and variations in human motion. Although exhaustive quantitative evaluations are beyond the scope of this section, the observed stable navigation behavior in real indoor environments suggests that the proposed framework exhibits promising sim-to-real transfer capability. These results further indicate that the proposed 5D risk features serve as robust signals for control arbitration, enabling the robot to remain within the desired following region while maintaining safety in noisy and non-stationary conditions.

6. Conclusion

The work presented ARMS, a hybrid learning–control framework for safe human–robot cooperative base navigation. ARMS combines a PPO-trained follower with a hand-crafted one-step MPC-formulated QP safety filter through a learned, adaptive switcher. The follower operates on a compact observation built from ring-encoded 360° LiDAR, provided either as raw beams or as a frozen 32-D latent embedding from a NavRep-style encoder, augmented with short-term temporal encoding via an LSTM. The switcher maps a compact set of risk features to a continuous fusion weight $\alpha \in [0, 1]$ and executes a convex combination of the follower and safety-filter actions. This design yields smooth, context-aware arbitration: it transitions between efficient tracking in benign regions and follower-dominant reactions under tight clearances, while the QP safety filter provides conservative, feasibility-aware corrective actions when the optimization is feasible. We evaluated ARMS in a trajectory-replay simulation driven by synthetically generated operator trajectories with obstacle factors of varying difficulty, and compared against DWA, a 1-step QP safety-filter-only baseline, and a PPO-only follower under identical observations and actuation limits. Across cluttered scenarios, ARMS improves success and safety outcomes while maintaining real-time control. We further validated the approach in Gazebo and on a physical robot platform, indicating that the learned follower and switcher remain functional under more realistic sensing and dynamics. Future work will focus on deployment on physical mobile bases, incorporating delay and noise modeling and broader

domain randomization to improve transfer, and investigating richer risk and safety constraints, including extensions to moving obstacles and multi-human scenarios.

References

- [1] Phani Teja Singamaneni, Pilar Bachiller-Burgos, Luis J. Manso, Anaís Garrell, Alberto Sanfeliu, Anne Spalanzani, and Rachid Alami. A survey on socially aware robot navigation: Taxonomy and future challenges. *The International Journal of Robotics Research*, 2024. doi: 10.1177/02783649241230562.
- [2] Christoforos I. Mavrogiannis, Francesca Baldini, Allan Wang, Dapeng Zhao, Pete Trautman, Aaron Steinfeld, and Jean Oh. Core challenges of social robot navigation: A survey. *ACM Transactions on Human-Robot Interaction*, 12(3), 2023. doi: 10.1145/3583741.
- [3] Yuwen Liao, Xinhang Xu, Ruofei Bai, Yizhuo Yang, Muqing Cao, Sheng-hai Yuan, and Lihua Xie. Following is all you need: Robot crowd navigation using people as planners, 2025.
- [4] Ye Zhang, Wang Zhao, Jingyu Wang, and Yuan Yuan. Recent progress, challenges and future prospects of applied deep reinforcement learning: A practical perspective in path planning. *Neurocomputing*, 608:128423, December 2024. doi: 10.1016/j.neucom.2024.128423.
- [5] Xiaoshuang Li, Xiao Wang, Xinhua Zheng, Junchen Jin, Yanhao Huang, Jun Jason Zhang, and Fei-Yue Wang. SADRL: Merging human experience with machine intelligence via supervised assisted deep reinforcement learning. *Neurocomputing*, 467:300–309, January 2022. doi: 10.1016/j.neucom.2021.09.064.
- [6] Enrico Fiasch , Philippe Martinet, and Ezio Malis. Towards autonomous robot navigation in human populated environments using an universal SFM and parametrized MPC. In *IEEE/RSJ International Conference on Intelligent Robots and Systems*, pages 7422–7427, 2023. doi: 10.1109/IROS55552.2023.10341814.
- [7] Haoge Jiang, Mahdi Abolfazli Esfahani, Keyu Wu, Kong wah Wan, Kuan kian Heng, Han Wang, and Xudong Jiang. itd3-cln: Learn to navigate

in dynamic scene through deep reinforcement learning. *Neurocomputing*, 503:118–128, September 2022. doi: 10.1016/j.neucom.2022.06.102.

- [8] Zhanteng Xie and Philip M. Dames. DRL-VO: Learning to navigate through crowded dynamic scenes using velocity obstacles. *IEEE Transactions on Robotics*, 39(4):2700–2719, 2023. doi: 10.1109/TRO.2023.3257549.
- [9] Wen-Hua Chen. Perspective view of autonomous control in unknown environment: Dual control for exploitation and exploration vs reinforcement learning. *Neurocomputing*, 497:50–63, August 2022. doi: 10.1016/j.neucom.2022.04.131.
- [10] Lukas Brunke, Melissa Greeff, Adam W. Hall, Zhaojian Yuan, Sihao Zhou, Jacopo Panerati, and Angela P. Schoellig. Safe learning in robotics: From learning-based control to safe reinforcement learning. *Annual Review of Control, Robotics, and Autonomous Systems*, 5:411–444, 2022. doi: 10.1146/annurev-control-042920-020211.
- [11] Thibault Kruse, Amit Kumar Pandey, Rachid Alami, and Alexandra Kirsch. Human-aware robot navigation: A survey. *Robotics and Autonomous Systems*, 61(12):1726–1743, 2013.
- [12] Weitian Wang, Rui Li, Yi Chen, Z. Max Diekel, and Yunyi Jia. Facilitating human–robot collaborative tasks by teaching–learning–collaboration from human demonstrations. *IEEE Transactions on Automation Science and Engineering*, 16(2):640–653, 2019. doi: 10.1109/TASE.2018.2840345.
- [13] Andrea Casalino, Andrea Maria Zanchettin, Luigi Piroddi, and Paolo Rocco. Optimal scheduling of human–robot collaborative assembly operations with time petri nets. *IEEE Transactions on Automation Science and Engineering*, 18(1):70–84, 2021. doi: 10.1109/TASE.2019.2932150.
- [14] Peter Trautman and Andreas Krause. Unfreezing the robot: Navigation in dense, interacting crowds. In *IEEE/RSJ International Conference on Intelligent Robots and Systems*, pages 797–803. IEEE, 2010.
- [15] Linzhuo Pang, Yunzhou Zhang, Sonya Coleman, and He Cao. Efficient hybrid-supervised deep reinforcement learning for person following robot.

Journal of Intelligent & Robotic Systems, 97:299–312, 2020. doi: 10.1007/s10846-019-01030-0.

- [16] Luca Scofano, Alessio Sampieri, Tommaso Campari, Valentino Sacco, Indro Spinelli, Lamberto Ballan, and Fabio Galasso. Following the human thread in social navigation, 2024.
- [17] Henrik Kretzschmar, Markus Spies, Christoph Sprunk, and Wolfram Burgard. Socially compliant mobile robot navigation via inverse reinforcement learning. *The International Journal of Robotics Research*, 35(11):1289–1307, 2016.
- [18] Daniel Rodriguez-Criado, Pilar Bachiller-Burgos, Luis J. Manso, Pablo Bustos, and Diego R. Faria. SNGNN2D-v2: A GNN-based model for the generation of human-aware cost maps in dynamic environments. *International Journal of Social Robotics*, 2024. doi: 10.1007/s12369-024-01190-6.
- [19] Haresh Karnan, Anirudh Nair, Xuesu Xiao, Garrett Warnell, Soeren Pirk, Alexander Toshev, Justin Hart, Joydeep Biswas, and Peter Stone. SCAND: Socially compliant navigation dataset: A large-scale dataset of demonstrations for social navigation, 2022.
- [20] Linh Kästner, Volodymyir Shcherbyna, Huajian Zeng, Tuan Anh Le, Maximilian Ho-Kyoung Schreff, Halid Osmaev, Nam Truong Tran, Diego Diaz, Jan Golebiowski, Harold Soh, and Jens Lambrecht. Arena 3.0: Advancing social navigation in collaborative and highly dynamic environments, 2024.
- [21] Sertac Karaman and Emilio Frazzoli. Sampling-based algorithms for optimal motion planning. *The International Journal of Robotics Research*, 30(7):846–894, 2011.
- [22] Zhiqiang Jian, Songyi Zhang, Lingfeng Sun, Wei Zhan, Nanning Zheng, and Masayoshi Tomizuka. Long-term dynamic window approach for kinodynamic local planning in static and crowd environments. *IEEE Robotics and Automation Letters*, 8(6):3294–3301, 2023. doi: 10.1109/LRA.2023.3266664.
- [23] Luca Mozzarelli, Matteo Corno, and Sergio Matteo Savaresi. Socially aware local planning: a dynamic window-based approach. In *European*

Control Conference, pages 3255–3260, 2024. doi: 10.23919/ECC64448. 2024.10591069.

- [24] Hasan Kivrak, Furkan Cakmak, Hatice Kose, and Sirma Yavuz. Social navigation framework for assistive robots in human inhabited unknown environments. *Engineering Science and Technology, an International Journal*, 24(2):284–298, 2021. doi: 10.1016/j.jestch.2020.08.008.
- [25] Timur Akhtyamov, Aleksandr Kashirin, Aleksey Postnikov, Ivan Sosin, and Gonzalo Ferrer. Social robot navigation through constrained optimization: A comprehensive study of uncertainty-based objectives and constraints in the simulated and real world. *Robotics and Autonomous Systems*, 183:104830, 2025. doi: 10.1016/j.robot.2024.104830.
- [26] Adarsh Jagan Sathyamoorthy, Utsav Patel, Tianrui Guan, and Dinesh Manocha. Frozone: Freezing-free, pedestrian-friendly navigation in human crowds. *IEEE Robotics and Automation Letters*, 5(3):4352–4359, 2020. doi: 10.1109/LRA.2020.2996593.
- [27] Jur Van Den Berg, Stephen J Guy, Ming Lin, and Dinesh Manocha. Reciprocal n-body collision avoidance. In *Robotics Research: The International Symposium ISRR*, pages 3–19. Springer, 2011.
- [28] John Schulman, Filip Wolski, Prafulla Dhariwal, Alec Radford, and Oleg Klimov. Proximal policy optimization algorithms, 2017.
- [29] Timothy P. Lillicrap, Jonathan J. Hunt, Alexander Pritzel, Nicolas Heess, Tom Erez, Yuval Tassa, David Silver, and Daan Wierstra. Continuous control with deep reinforcement learning, 2015.
- [30] Adarsh Jagan Sathyamoorthy, Utsav Patel, Moumita Paul, Nithish K. Sanjeev Kumar, Yash Savle, and Dinesh Manocha. CoMet: Modeling group cohesion for socially compliant robot navigation in crowded scenes. *IEEE Robotics and Automation Letters*, 7(2):1008–1015, 2022. doi: 10.1109/LRA.2021.3135560.
- [31] Zhen Feng, Bingxin Xue, Chaoqun Wang, and Fengyu Zhou. Safe and socially compliant robot navigation in crowds with fast-moving pedestrians via deep reinforcement learning. *Robotica*, 42(4):1212–1230, 2024. doi: 10.1017/S0263574724000183.

- [32] Estrella Montero, Nabih Pico, Mitra Ghergherehchi, and Ho Seung Song. Memory-driven deep-reinforcement learning for autonomous robot navigation in partially observable environments. *Engineering Science and Technology, an International Journal*, 62:101942, 2025. doi: 10.1016/j.jestch.2024.101942.
- [33] Aaron D Ames, Xiangru Xu, Jessy W Grizzle, and Paulo Tabuada. Control barrier function based quadratic programs for safety critical systems. *IEEE Transactions on Automatic Control*, 62(8):3861–3876, 2016.
- [34] Gal Dalal, Krishnamurthy Dvijotham, Matej Vecerik, Todd Hester, Cosmin Paduraru, and Yuval Tassa. Safe exploration in continuous action spaces. *arXiv preprint arXiv:1801.08757*, 2018.
- [35] M. Dawood, A. Shokry, and M. Bennewitz. A dynamic safety shield for safe and efficient reinforcement learning of navigation tasks, 2024.
- [36] Ning Liu, Sen Shen, Xiangrui Kong, Hongtao Zhang, and Thomas Bräunl. Cooperative hybrid multi-agent pathfinding based on shared exploration maps. *Journal of Intelligent & Robotic Systems*, 111(3):97, 2025.
- [37] Peter E. Hart, Nils J. Nilsson, and Bertram Raphael. A formal basis for the heuristic determination of minimum cost paths. *IEEE Transactions on Systems Science and Cybernetics*, 4(2):100–107, 1968. doi: 10.1109/TSSC.1968.300136.
- [38] Xiangrui Kong, Thomas Braunl, Marco Fahmi, and Yue Wang. A superalignment framework in autonomous driving with large language models. In *2024 IEEE Intelligent Vehicles Symposium (IV)*, pages 1715–1720. IEEE, 2024.
- [39] Xiangrui Kong, Li Liang, Jichuiyang Li, Kieran Quirke-Brown, Zhihui Lai, Doina Olaru, and Thomas Bräunl. A generative self-diagnosis disengagement reporting system for autonomous shuttles. In *2025 IEEE Intelligent Vehicles Symposium (IV)*, pages 716–721. IEEE, 2025.
- [40] Daniel Dugas, Juan Nieto, Roland Siegwart, and Jen Jen Chung. NavRep: Unsupervised representations for reinforcement learning of robot navigation in dynamic human environments. In *IEEE International Con-*

ference on Robotics and Automation, pages 7829–7835, 2021. doi: 10.1109/ICRA48506.2021.9560951.